Structural Changes in Atomically Precise Ag_{29} Nanoclusters upon Sequential Attachment and Detachment of Secondary Ligands

Jayoti Roy, Amitabha Das, Arijit Jana, Papri Chakraborty, Marco Neumaier, Horst Hahn, Biswarup Pathak,* Manfred M. Kappes,* and Thalappil Pradeep*

ABSTRACT: Elucidating the structural dynamics of ligand-stabilized noble metal nanoclusters (NCs) is critical for understanding their properties and for developing applications. Ligand rearrangement at NC surfaces is an important contributor to structural change. In this study, we investigate the dynamic behavior of ligand-protected $[Ag_{29}(L)_{12}]^{3-}$ NC's (L = 1,3-benzenedithiol) interacting with secondary ligand 2,2′-[1,4-phenylenebis(methylidynenitrilo)] bis[benzenethiol] (referred to as L′). We specifically focus on the structural characteristics of NC-based adducts $[Ag_{29}(L)_{12}]L'_n{}^{3-}$ where n ranges from 1 to 4. This is probed experimentally by using a combination of ultraviolet−visible (UV−vis) spectroscopy, high-resolution electrospray ionization mass spectrometry (ESI MS), and ion mobility mass spectrometry (IM MS) coupled with collision-induced dissociation (MS^2 IMS). Density functional theory (DFT) calculations infer comparatively weak noncovalent interactions between the NCs and attached secondary ligands consistent with the fragmentation behavior and experimentally determined collision cross-sections (CCSs), which show a monotonic CCS increase of $[Ag_{29}(L)_{12}]L'_n{}^{3-}$ with an increasing number of L′ (n = 1−4). From a detailed analysis of the predicted structures, we infer progressive expansion of the Ag−S staple framework of the precursor NC as secondary ligands are added. Interestingly, detachment of L′ from gas-phase $[Ag_{29}(L)_{12}]L'_n{}^{3-}$ by collisional heating yields structures which retain "footprints" of the detached secondary ligands on a millisecond time scale.

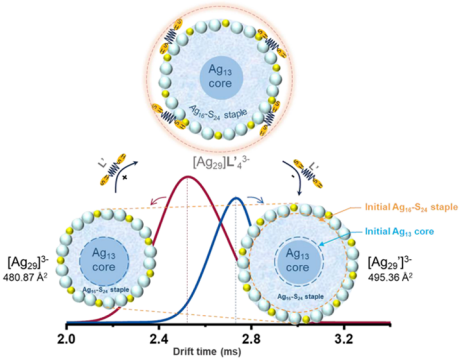

KEYWORDS: *atomically precise noble metal nanoclusters, Ag_{29} nanocluster, structural isomerism, supramolecular interactions, secondary ligand interaction, ion mobility mass spectrometry, DFT calculation*

INTRODUCTION

Atomically precise, ligand-protected, noble metal nanoclusters (NCs) are an exceptional class of ultrasmall nanoparticles that are composed of metal atoms and organic ligands.[1−3] These metallic nanostructures have potential applications as catalysts,[4,5] agents for biological imaging and sensing,[6,7] and tunable nanomaterials for diagnostics and therapeutics.[8] The properties of these materials depend strongly on their size due to their distinct molecular electronic levels.[9−11]

Determination of the molecular structures of NCs by single-crystal X-ray diffraction (SCXRD) has been a major driver of progress in this area.[12,13] Numerous structures have been resolved since the first reported crystal structure of a thiolate-protected gold NC, $Au_{102}(pMBA)_{44}$ (where pMBA = *p*-mercaptobenzoic acid).[14] Later, structures of Au and Ag NCs and, to a limited extent, Cu and other metal alloy NCs protected by various ligands such as thiolates, phosphines, alkynyls, or N-heterocyclic carbenes and carboranes have been solved.[3,15−22] Although SCXRD is a proven technique to determine the structure of monolayer-protected coinage metal NCs in the solid state, it is still challenging to characterize NC structures in solution and gas phases.[23,24] NCs can become quite dynamic when freed from their crystalline lattice. For example, it has been shown that $[Au_{25}(PET)_{18}]$ NC ions can exist in dimeric and trimeric aggregate states in the gas phase, whereas a chiral NC, such as $Au_{38}(PET)_{24}$ (PET = phenylethanethiolate), can even invert its handedness in solution.[25,26] Such dynamic phenomena are known to depend strongly on the nature of the surface layer of NC. In thiolate-

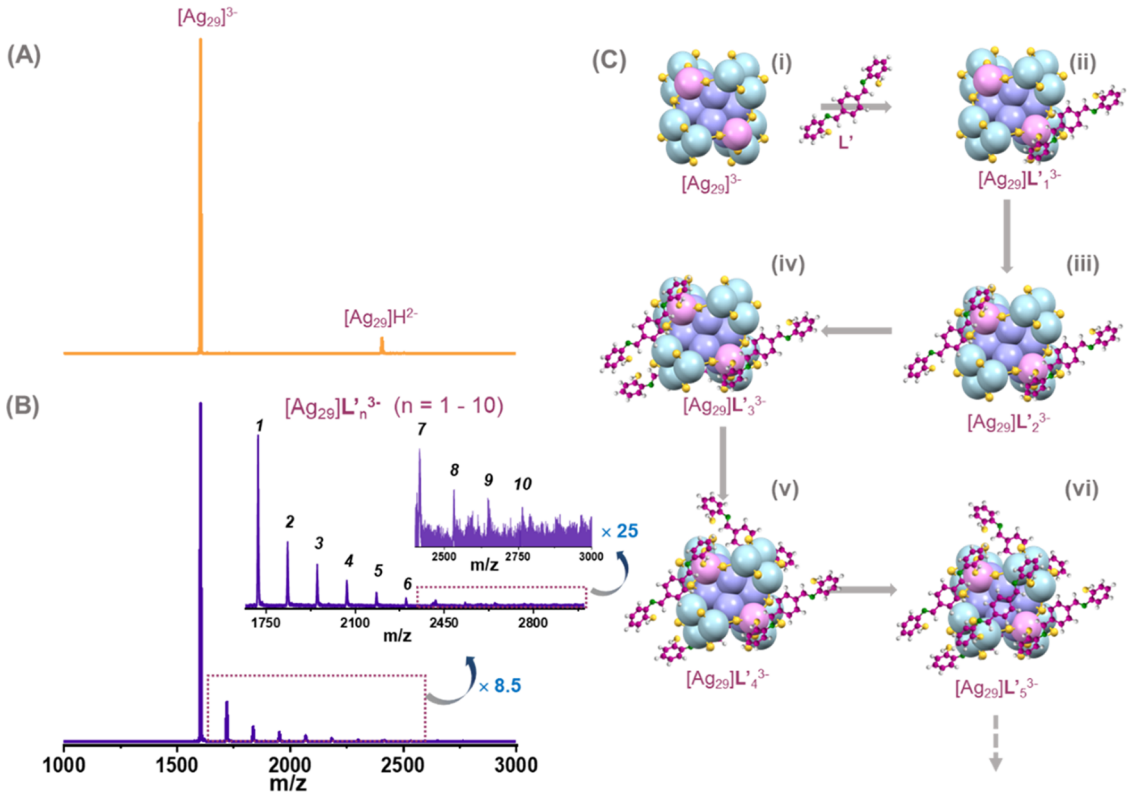

Figure 1. Partial ESI MS of (A) precursor $[Ag_{29}]^{3-}$ NC solution and (B) precursor NC solution with L′ added (in the DMF solvent). (C) Schematic of the proposed reaction sequence generating $[Ag_{29}]L'_n{}^{3-}$ NCs by sequential addition of L′. Color code: Ag, purple, pink, and cyan blue; S, yellow; C, dark magenta; H, light gray; and N, dark green.

protected coinage metal NCs, for example, the ligands are covalently attached to metal−thiolate staples, which together constrain the metallic cluster core. One of the conceptually simplest solution reactions of such a system involves the interaction of the NC thiolate surface layer with a secondary ligand. Surprisingly though, the secondary ligand-induced chemical properties of NCs have only been explored to a limited extent.[27−30] Contributing effects include (i) host−guest interactions with the primary ligands,[23] (ii) rearrangement of the metal−thiolate interface,[33−35] (iii) modulation of the primary ligand binding affinity by incoming molecules,[36−38] and (iv) flexibility of the metal(I)-thiolate staples.[31,34,39] All of these processes are likely to involve multiple intermediates, i.e., isomeric structures. However, there are few experimental data on isomers formed during the interaction of the metal−thiolate framework with foreign molecules.

Understanding the structural dynamics of NC structures therefore has also been greatly profited from computational modeling, in addition to experiments.[40,41] For example, Matus et al. explored the possibilities of isomerism in the Au_{13} core of $[Au_{25}(SR)_{18}]$ NCs using MD and density functional theory (DFT) studies. The MD-simulated Au_{13} core was shown to differ structurally from that known in the crystal by a low-barrier collective rotation.[42] This study revealed that topological isomers of isolated $[Au_{25}(SR)_{18}]^-$ have distinctly different collision cross-sections (CCS) as compared to the known solid-state structures, emphasizing the need and importance of gas-phase ion mobility-mass spectrometry (IM MS) studies to better elucidate structural dynamics, which is also relevant in the solution phase.

IM MS, in combination with theoretical calculations, has been used extensively to assign gas-phase structures of large biomolecular ions, NCs, proteins, etc.[43−45] Also, the combination of IM MS with collisional fragmentation (MS^2 IMS) has become an indispensable tool for identifying structural changes.[46−53] This approach has been applied recently to explore possible isomeric structures of coinage metal NCs in the gas phase and to follow their structural changes during chemical reactions.[39,48,54,55] Often, the results from high-resolution IM MS have been validated by SCXRD. For NCs, the reliability of IM MS-based structural assignment has been evidenced in the literature by comparing such results with known X-ray structures.[56] Soleilhac et al. used IM MS to determine the CCSs of a series of gold NCs protected by glutathione and demonstrated that the relative changes in CCSs in the gas phase were consistent with the results from powder XRD in the solid phase and time-resolved fluorescence anisotropy in the liquid phase.[40] Advanced IM MS techniques, such as high-resolution trapped ion mobility spectrometry (TIMS) MS, in combination with DFT, were used to resolve smaller changes in the CCS resulting from Cu doping in different positions of the $[Ag_{29}(L)_{12}]^{3-}$ NC (L = 1,3-benzenedithiol).[56] Notably, structures of several NCs, such as $[Au_7(PPh_3)_7H_5]^{2+}$ and $[Au_8(PPh_3)_7]^{2+}$, have even been assigned purely based on the agreement between the experimental and calculated CCS values.[57]

In this study, we use electrospray ionization MS (ESI MS) and IM MS to explore structural dynamics and isomerism associated with the interaction of the $[Ag_{29}(L)_{12}]^{3-}$ silver-thiolate NC model system (where L corresponds to 1,3-benzene-dithiol) with the secondary ligand, 2,2′-[1,4-phenyl-

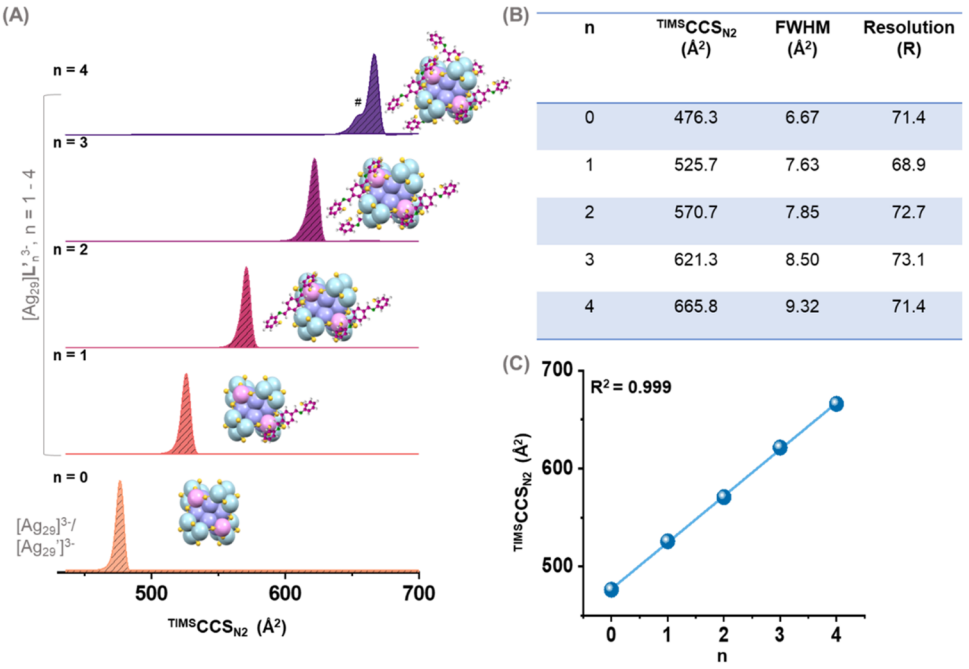

Figure 2. (A) Mobilograms of individual $[Ag_{29}]L'_n{}^{3-}$ (n = 0−4) ions showing increasing CCS with an increasing number of L′-adducts to $[Ag_{29}]^{3-}$ NCs. (B) Table showing the $^{TIMS}CCS_{N2}$, FWHM, and resolution (R) values corresponding to the number of L′-ligands (n) attached to parent $[Ag_{29}]^{3-}$ NCs. (C) Linear correlation plot of $^{TIMS}CCS_{N2}$ versus n. Color code: Ag, purple, pink, and cyan blue; S, yellow; C, dark magenta; H, light gray; and N, dark green. # marks that the ions of lower CCS than $[Ag_{29}]L'_4{}^{3-}$ could be attributed to either fragmentation or artifact during elution from the TIMS tunnel of timsTOF.

enebis (methylidynenitrilo)]bis[benzenethiol] (denoted as **L′**). Mixing **L′** with $[Ag_{29}(L)_{12}]^{3-}$ NC solution leads to the formation of weakly bound adduct ions $[Ag_{29}(L)_{12}]L'_n{}^{3-}$ (n = 1−4). This is associated with a monotonic increase in their overall size as **L′** is added. Collisional dissociation (CID) of these adducts leads to the sequential detachment of (neutral) **L′** as the lowest-energy fragmentation channel. Surprisingly, the resulting fragment ions have larger collision cross-sections than the corresponding (unfragmented) equi-m/z ions directly electrosprayed from solution. DFT calculations[58] as well as trajectory method simulations of CCS values for plausible model structures[59] provide insights into the underlying structure changes and show that they reflect specific noncovalent interactions between secondary ligands and NC. These results are described in detail in the following where we will abbreviate $[Ag_{29}(L)_{12}]^{3-}$ as $[Ag_{29}]^{3-}$ and $[Ag_{29}(L)_{12}]L'_n{}^{3-}$ as $[Ag_{29}]L'_n{}^{3-}$, respectively.

The $[Ag_{29}](TPP)_4{}^{3-}$ NC solid with counterions (TPP is triphenylphosphine) and secondary ligand, **L′**, were synthesized using reported protocols (see the Experimental Section in the Supporting Information) and characterized by high-resolution ESI MS (Figure S1), ultraviolet−visible (UV−vis) absorption spectroscopy, and photoluminescence spectroscopy (Figure S2).[60] The negative ion ESI mass spectrum of a $[Ag_{29}](TPP)_4{}^{3-}$ solution displays two NC-derived ion signals in two different charge states, predominantly 3- (as $[Ag_{29}]^{3-}$) and also some 2- (as $[Ag_{29}]H^{2-}$). Each forms after losing four weakly bound neutral TPP ligands (Figure S1). Under our ESI MS conditions, the relative dianionic intensity was less than 5% of the total ion count. The expanded isotopic distribution of the major peak (i.e., trianionic) in the mass spectrum is in agreement with the calculated isotopic distribution, as shown in Figure S1C, thus demonstrating sample purity. Upon introduction of **L′** (0.026 mM) into a ∼ 50 μM DMF−methanol solution of $[Ag_{29}]^{3-}$ at room temperature (∼298 K), $[Ag_{29}]L'_n{}^{3-}$ adducts (n = 1−10) were observed to form faster than 30 s after mixing (corresponding to the apparatus dead time before ESI MS detection) as shown in Figure 1B(i−ii). The concentrations of **L′** and $[Ag_{29}]^{3-}$ NC were fixed at an optimal concentration, which was arrived at by concentration-dependent measurements. At higher concentrations of **L′**, larger aggregates were formed and a study of the same will be reported in the future.

Many other studies have shown that ESI MS can yield a good relative measure of the composition of solutions of charged, atomically precise NCs. On the basis of the ratio of mass spectral peak intensity for $[Ag_{29}]^{3-}$ to the sum of $[Ag_{29}]L'_n{}^{3-}$ signals, we infer that roughly 15% of the parent ions form adducts in solution (or during ESI). Accurate mass measurements confirmed that adduct ions were separated by ∼ m/z 116, corresponding to the addition of **L′** (mass of **L′** is 348, i.e., 116 × 3). Therefore, structural integrity of **L′** appears maintained upon binding to the NC (i.e., no loss of small fragments such as H or H_2). This is consistent with a comparison of the UV−vis spectrum of the mixed solution with that of pure $[Ag_{29}](TPP)_4{}^{3-}$ NC and the pure secondary ligand, **L′**. The spectrum changes additively upon mixing. Similar changes were observed during photoluminescence studies upon luminating the solution at 445 nm. Upon increasing the concentration of **L′** to the NC solution, no apparent shift in the photoluminescence spectrum of $[Ag_{29}](TPP)_4{}^{3-}$ (at 660 nm) was observed.

Under the ESI conditions used to study the mixed solutions (after adding **L′**), the relative dianionic intensity was below the detection limit (peak intensity of $[Ag_{29}]H^{2-}$ (m/z 2405) was masked by the isotopic distribution of $[Ag_{29}]L'_7{}^{3-}$, m/z 2415).

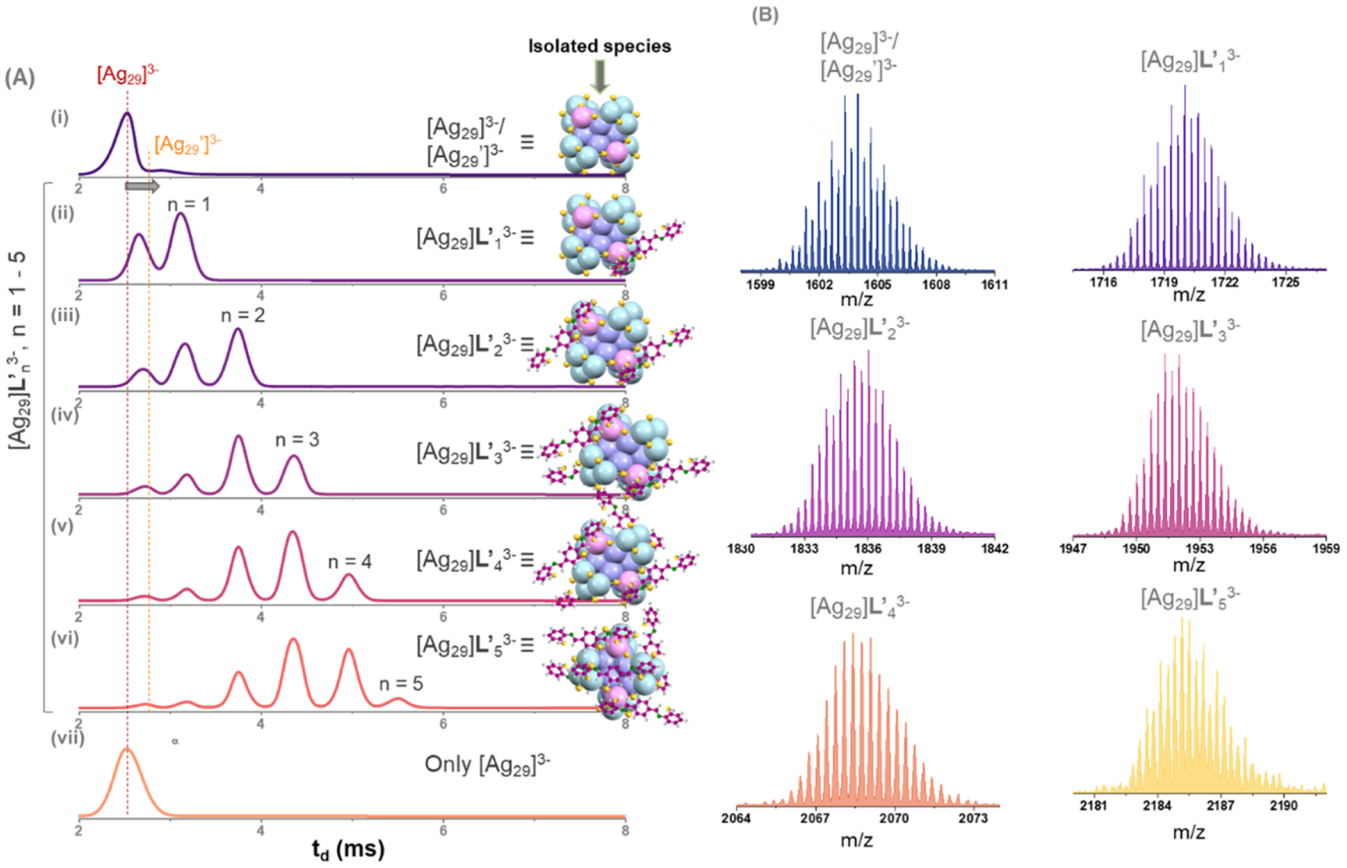

Figure 3. (A) (i–vi) Drift time measurements of mass-selected NC (complex) ions, $[Ag_{29}]L'_n{}^{3-}$ (n = 0–5) as sprayed from a solution of $[Ag_{29}]^{3-}$ and L′; (vii) reference drift time measurement for $[Ag_{29}]^{3-}$ sprayed from a pure $[Ag_{29}]^{3-}$ NC solution. Dotted lines indicate the shift in drift time from $[Ag_{29}]^{3-}$ toward a higher value for $[Ag_{29}']^{3-}$ (see text and Figure S4). (B) Extracted MS for individual peaks in the ATDs of $[Ag_{29}]L'_n{}^{3-}$ allowing the indicated assignment of the corresponding t_d values to specific parents and fragments (as also checked by comparing experimental and simulated isotopic distributions).

We therefore confine further discussion below to the trianions. The mass spectrum is consistent with the sequential addition of L′ to $[Ag_{29}]^{3-}$ NC as schematically depicted in Figure 1C. While signals of $[Ag_{29}]L'_n{}^{3-}$, $n \leq 4$, were quite stable, the intensity of ions with $n \geq 5$ decreased over time, suggesting a secondary process leading to a shift in solution equilibrium favoring smaller complexes. Therefore, only $[Ag_{29}]L'_n{}^{3-}$ complexes with n values from 1 to 4 are considered here (see Figure 1B(ii)).

IM MS was next employed to characterize the structure of the $[Ag_{29}]L'_n{}^{3-}$ complexes as well as to examine the influence of complexation on the NC precursor by using both timsTOF and Synapt IMS mass spectrometers.

Experimental CCS of $[Ag_{29}]^{3-}$ and $[Ag_{29}]L'_n{}^{3-}$ Ions. *TimsTOF Measurements.* $[Ag_{29}]^{3-}$ and $[Ag_{29}]L'_n{}^{3-}$ NC ions were monitored with high-resolution trapped ion mobility spectrometry in nitrogen collision gas (IMS MS) using procedures which we have described previously.[61−63] This results in calibrated collision cross-sections, which we denote as $^{TIMS}CCS_{N2}$. Figure 2A shows typical mobilograms (detected ion intensity versus $^{TIMS}CCS_{N2}$). The small peak labeled with # could be attributed to either fragmentation or artifact due to the nature of these weak adducts. $^{TIMS}CCS_{N2}$, full width at half maximum (FWHM, Å^2), and resolution (R) of individual ions are listed in Figure 2B and plotted versus n in Figure 2C. From this, we see that (i) within the CCS resolution obtainable, there is only one peak in each case (i.e., only one resolvable $[Ag_{29}]L'_n{}^{3-}$ isomer) and (ii) $^{TIMS}CCS_{N2}$ values increase linearly with the number of L′ added. The relative deviation in $^{TIMS}CCS_{N2}$ values of the NCs was <0.2% upon repeated measurements with the same instrumental conditions.[62]

Synapt Measurements. To further explore the dynamics of structural transformations upon reaction with secondary ligands, we performed systematic MS^2 IMS experiments on all isolated $[Ag_{29}]L'_n{}^{3-}$ (n = 0–5) using the Synapt instrumental platform.

The Synapt platform ensures that ions can be m/z-selected before the IMS measurement, thus also allowing for IMS studies of fragment ions. Fragments can be controllably formed during injection of m/z-selected species into the traveling wave ion mobility (TWIMS) cell with a selected collision energy (CE).[64,65] A TOF MS subsequently (re)analyzes the ions transmitted through the TWIMS, and as a result, tandem MS measurements combined with IMS analysis can be carried out: MS^2 IMS. Specifically, we applied a CE setting of 10 V to the trap cell, which leads only to the sequential loss of neutral secondary ligands from mass-selected $[Ag_{29}]L'_n{}^{3-}$ without causing additional fragmentation of the component NC, reaction 1.

Table 1. $^{TW}CCS_{N2}$ of Parent Ions ($[Ag_{29}]^{3-}$ and $[Ag_{29}]L'_n{}^{3-}$) and Fragment Ions Corresponding to Loss of m L′ Secondary Ligands ($[Ag_{29}]L'_{n-m}{}^{3-}$)—as Generated by Collisions Upon Injection of Parent Ions into the Triwave Sector of the Synapt IMS MS (See Text for Details)

Selected ions → / Gas phase fragment ions ↓	$[Ag_{29}]^{3-}$ $^{TW}CCS_{N2}$ (Å²)	$[Ag_{29}]L'_1{}^{3-}$ $^{TW}CCS_{N2}$ (Å²)	$[Ag_{29}]L'_2{}^{3-}$ $^{TW}CCS_{N2}$ (Å²)	$[Ag_{29}]L'_3{}^{3-}$ $^{TW}CCS_{N2}$ (Å²)	$[Ag_{29}]L'_4{}^{3-}$ $^{TW}CCS_{N2}$ (Å²)	$[Ag_{29}]L'_5{}^{3-}$ $^{TW}CCS_{N2}$ (Å²)
$[Ag_{29}']^{3-}$	480.9	488.6	492.8	494.7	494.8	495.4
$[Ag_{29}]L'_1{}^{3-}$	-	536.6	540.5	542.4	542.9	542.6
$[Ag_{29}]L'_2{}^{3-}$	-	-	597.2	598.3	598.1	598.3
$[Ag_{29}]L'_3{}^{3-}$	-	-	-	652.9	651.8	652.5
$[Ag_{29}]L'_4{}^{3-}$	-	-	-	-	704.7	705.0
$[Ag_{29}]L'_5{}^{3-}$	-	-	-	-	-	748.7

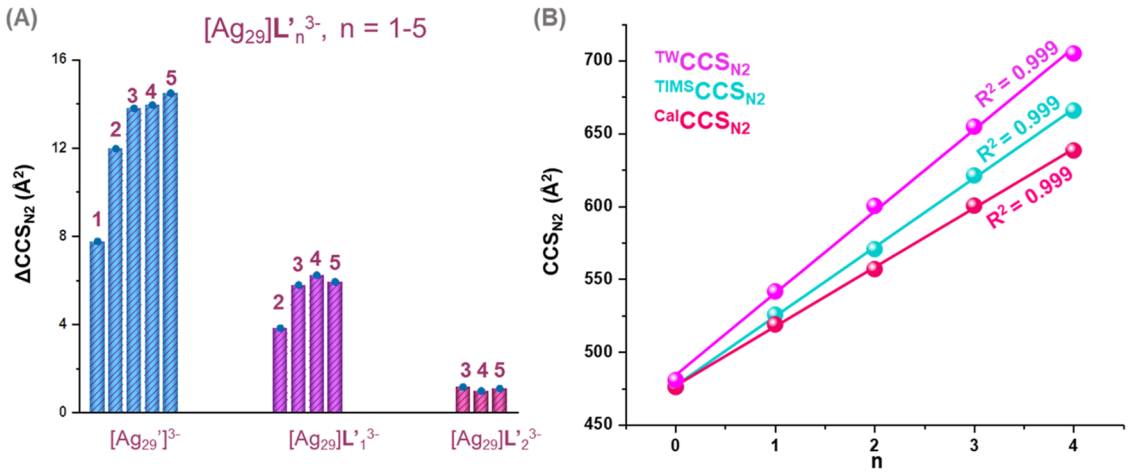

Figure 4. (A) Trend of ΔCCS values, calculated as the difference between the $^{TW}CCS_{N2}$ of parent ions and the $^{TW}CCS_{N2}$ of equi-m/z fragment species generated from higher adducts. (B) Theoretical ($^{Cal}CCS_{N2}$) and experimental CCS_{N2} ($^{TIMS}CCS_{N2}$ and $^{TW}CCS_{N2}$) of the parent and ligand added NC ions ($[Ag_{29}]^{3-}$, $[Ag_{29}']^{3-}$, and $[Ag_{29}]L'_n{}^{3-}$, n = 1−4) at ∼300 K. Note that while there is a linear dependence of CCS on n for both $^{TW}CCS_{N2}$ and $^{TIMS}CCS_{N2}$, slopes differ because of different calibration procedures.

$$[Ag_{29}]\mathbf{L}'_n{}^{3-*} \rightarrow [Ag_{29}]\mathbf{L}'_{n-1}{}^{3-} + \mathbf{L}' \rightarrow [Ag_{29}]\mathbf{L}'_{n-2}{}^{3-} + \mathbf{L}'\text{... so on (*represents the energetically excited } [Ag_{29}]\mathbf{L}'_n{}^{3-}\text{ions)} \quad (1)$$

Figure 3A, (i)−(vii), shows the resulting stacked mobilograms. This plot (overall injected ion signal intensity versus drift times, t_d) for all mass-selected $[Ag_{29}]\mathbf{L}'_n{}^{3-}$ was obtained after spraying from solution mixtures of $[Ag_{29}]^{3-}$ + L′ in comparison to the mobilogram of $[Ag_{29}]^{3-}$ recorded for a pure NC solution under the same instrumental settings. Drift times of features resolved in the heatmaps were correlated with the subsequent TOF mass analysis to yield "extracted MS". This allows to distinguish parent from fragment ions formed upon injection into the TWIMS cell. Figure 3B documents these extracted MS, which allowed us to assign the t_d features as labeled in (i)−(vi). From these, we have inferred that in the CE range probing all $[Ag_{29}]\mathbf{L}'_n{}^{3-}$ ($n > 0$) fragments according to reaction 1, i.e., there is no retention of thiol H atoms on the fragment multianions.

Interestingly, significant shifts in t_d between equi-m/z fragments (resulting from $[Ag_{29}]\mathbf{L}'_{n-m}{}^{3-}$ where m ranges up to 4) and unfragmented $[Ag_{29}]\mathbf{L}'_n{}^{3-}$ species indicate that the fragment ions have changed their structure. They are on average larger. This effect is further highlighted in the "heatmaps" shown in Figure S4A,B (ion signals versus t_d in milliseconds (ms), recorded for an m/z range around 1603 corresponding to $[Ag_{29}]^{3-}$ before and after introducing L′ to the solution). The peaks labeled with $[Ag_{29}]^{3-}$ in Figure S4A,B have essentially the same t_d value and can be attributed to the (unchanged) $[Ag_{29}]^{3-}$ parent ion. Introducing L′ into the solution leads to an additional peak in the heat map. This we interpret as a structural isomer of $[Ag_{29}]^{3-}$ generated through some gas-phase fragmentation of $[Ag_{29}]\mathbf{L}'_n{}^{3-}$ ($n > 0$) adducts

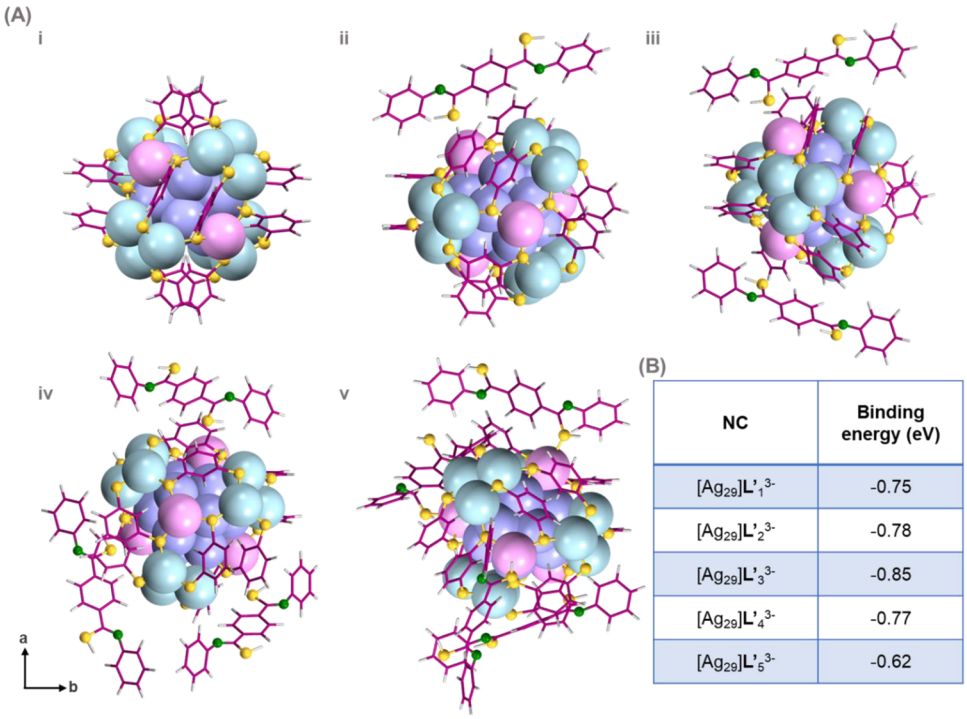

NC	Binding energy (eV)
$[Ag_{29}]L'_1{}^{3-}$	-0.75
$[Ag_{29}]L'_2{}^{3-}$	-0.78
$[Ag_{29}]L'_3{}^{3-}$	-0.85
$[Ag_{29}]L'_4{}^{3-}$	-0.77
$[Ag_{29}]L'_5{}^{3-}$	-0.62

Figure 5. (A) DFT-optimized structures of $[Ag_{29}]^{3-}$ NC (i) and its L′ complex ions $[Ag_{29}]L'_n{}^{3-}$ ions (n = 1−5; (ii) − (v)). (B) Table showing the calculated binding energy (per L′ attachment, in eV) of Color code: Ag, purple, pink, and cyan blue; S, yellow; C, dark magenta; H, light gray; and N, dark green.

by way of **L′** loss already prior to the initial mass selection. Again, this peak appears at a higher t_d (~2.9 ms) than the parent, suggesting significantly expanded structural isomers which we denote as $[Ag_{29}']^{3-}$ for further discussion below.

Thus, we infer an overall three-step process: (i) **L′** attachment to $[Ag_{29}]^{3-}$ in solution (or during ESI) to form $[Ag_{29}]L'_n{}^{3-}$ ($n > 0$) adducts, (ii) isolation of these adducts in the gas phase, and then (iii) soft collision-induced detachment of secondary ligands **L′** upon initiating the ion mobility measurement. Each ion mobility measurement was multiply repeated to confirm the reproducibility of the measured t_d values, and from these, the corresponding (calibrated) $^{TW}CCS_{N2}$ values were determined, which will be discussed next.

Table 1 shows the experimental $^{TW}CCS_{N2}$ values of the parent and fragment ions as determined by MS^2 IMS measurements (calibrated using reported methods).[66,67] The $^{TW}CCS_{N2}$ values were found to be stable across a range of activation conditions, indicating the structural stability of the ions (which are rapidly thermalized back down to room temperature at the beginning of their passage through the TWIMS cell). Specifically, the $^{TW}CCS_{N2}$ value for parent $[Ag_{29}]^{3-}$ was 480.9 Å^2, aligning closely with recently reported values.[56,66,67] Table 1 reveals a progressive increase in $^{TW}CCS_{N2}$ from left to right for the m/z ratio corresponding to $[Ag_{29}]^{3-}$ and $[Ag_{29}']^{3-}$ ($^{TW}CCS_{N2}$ (Å^2): 480.9 < 488.6 < 492.8 < 494.7 < 494.8 < 495.4), indicating progressive structural changes in $[Ag_{29}]^{3-}$ isomers formed by fragmentation of $[Ag_{29}]L'_n{}^{3-}$ (n = 1−5).

The detachment of **L′** ligands due to collisional excitation of $[Ag_{29}]L'_n{}^{3-}$ ($n > 0$) ions generally resulted in increased $^{TW}CCS_{N2}$ values relative to the unfragmented reference mass, independent of the $[Ag_{29}]L'_{n-m}{}^{3-}$ species formed as Figure 4A illustrates. This shows the extent of $^{TW}CCS_{N2}$ changes for fragment masses $[Ag_{29}']^{3-}$, $[Ag_{29}]L'_1{}^{3-}$, and $[Ag_{29}]L'_2{}^{3-}$, compared to the number of secondary ligands previously detached to generate them, e.g., a deviation of 1.7% is observed for $[Ag_{29}']^{3-}$ resulting from $[Ag_{29}]L'_1{}^{3-}$ (relative to the $^{TW}CCS_{N2}$ of the parent $[Ag_{29}]^{3-}$). Deviations become larger as more secondary ligands are lost to generate the fragment in question. Analogous but smaller effects are seen when analyzing the $[Ag_{29}]L'_1{}^{3-}$ or $[Ag_{29}]L'_2{}^{3-}$ fragment formation.

To put the impact of secondary **L′** ligands on the structural dynamics of the $[Ag_{29}]^{3-}$ NC into a wider context, analogous IMS MS experiments were also attempted with two other foreign ligands, namely 2-pyreneiminethiol (referred to as **L″**) and 1,6-hexanedithiol (denoted as **L‴**), separately. These two ligands (for structures, see Figure S5) were chosen because **L″** has a terminal group similar to **L′**, and **L‴** is a dithiol similar to **L′**. **L″** and **L‴** ligands were introduced separately into the $[Ag_{29}](TPP)_4{}^{3-}$ NC solution, followed by ESI MS and subsequent IMS MS measurements (see Figure S6). No additional peaks related to foreign ligand incorporation were observed in ESI MS for either case. Furthermore, IMS MS results showed no significant changes in the drift time (t_d) of the parent NC, indicating minimal impact on its structure (see Figure S6).

Density Functional Theory (DFT) and CCS Calculations by the Trajectory Method (TM). The interaction of secondary **L′** ligands with the $[Ag_{29}]^{3-}$ NC was studied computationally using DFT. First, structural optimization of the isolated $[Ag_{29}]^{3-}$ NC was performed starting from the previously reported crystal structure.[60] The calculated CCS for $[Ag_{29}]^{3-}$ NC was found to be 476.04 Å^2, which is comparable with our experimentally determined $^{TIMS}CCS_{N2}$ and $^{TW}CCS_{N2}$ values (those are 476.3 and 480.9 Å^2, respectively). The small difference can be rationalized by Ag not being specifically parametrized in IMoS (a general default setting is used

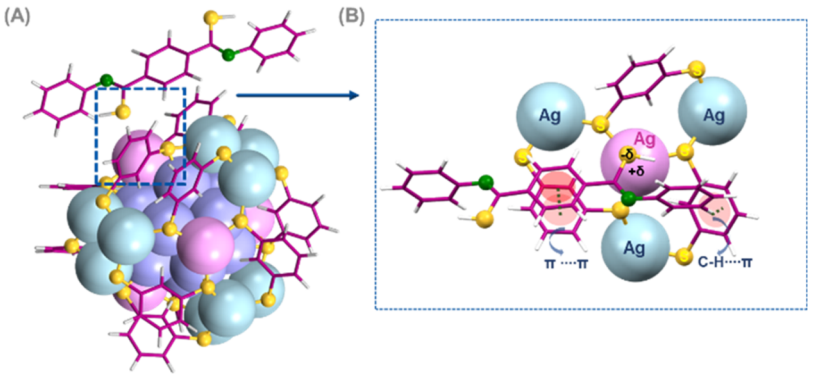

Figure 6. (A) DFT-optimized lowest-energy structure of $[Ag_{29}]L'_1{}^{3-}$ NC, highlighting the interaction of L′ ligand at the Ag atom at crown site. (B) Enlarged view of the staples around the crown Ag atom and peripheral tetrahedral Ag-L showing how three proximal L ligands (and associated Ag−S bonds) of the $[Ag_{29}]^{3-}$ NC are influenced by ionic, $\pi\cdots\pi$, and CH$\cdots\pi$ interactions with the attached L′ ligand. The partial ionic character associated with $[Ag_{29}]^{3-}$-L′ complexation is denoted by $\delta+$ / $\delta-$. Color code: Ag, purple, pink, and cyan blue; S, yellow; C, dark magenta, H, light gray; and N, dark green.

instead). This optimized $[Ag_{29}]^{3-}$ structure was then used as a starting point to model the secondary ligand addition (Figure 5A(i)). To rationally correlate plausible DFT-derived structural models, their corresponding $^{Cal}CCS_{N2}$ values were then calculated by using the trajectory method (TM) and compared to experimentally observed $^{TW}CCS_{N2}$ values of $[Ag_{29}]L'_n{}^{3-}$. Due to the large size of the system, we have not considered zero-point energy corrections for structural optimization.

Before the results are described, it is useful at this stage to further familiarize the reader with the structure of $[Ag_{29}]^{3-}$. The DFT-derived-optimized structure is very similar to the crystal structure, which manifests four distinct types of Ag atoms. These types encompass (see Figure S3) the central Ag atom positioned within the replete icosahedral core, the residual set of 12 Ag atoms constituting the icosahedral framework (icosahedral Ag), another 12 atoms directly bonded to the S atoms of the L ligands forming the NC thiolate shell (tetrahedral Ag (4 × 3)), and 4 undercoordinated Ag atoms (crown Ag) to each of which a PPh_3 ligand is bound in the solid (these are lost in the gas phase).[60] The 12 L ligands coordinate to 12 tetrahedral Ag atoms as bidentate thiols constituting the shell of the NC. Pairs of L ligands coexist on the surface of the NC due to the $\pi\cdots\pi$ interactions between parallel phenyl rings of Ls.

Both the regular ESI MS pattern of $[Ag_{29}]L'_n{}^{3-}$ adducts and the low CE threshold for **L′** detachment are consistent with comparatively weak supramolecular interactions between the secondary ligands and $[Ag_{29}]^{3-}$ NC. We therefore explored many possible noncovalent adducts of **L′**. We optimized the **L′** ligand in both its *cis* and trans forms using DFT in TURBOMOLE[68] with the B3-LYP functional[69−73] and the def2-TZVP[74] (valence triple-ζ polarization) basis set and accounting for dispersion at the D3(BJ)[75,76] level. We found a negligible relative energy difference between *cis*-**L′** and trans-**L′** of 0.0005 eV in favor of the trans-isomer (see Figure S7). Preliminary DFT calculations indicate a low rotational barrier (∼0.08 eV) and an easy interconversion between the two isomers at room temperature using the wB97X-V/def2-TZVP basis set with the r^{2}SCAN-3c method and the conductor-like polarizable continuum model (CPCM)-like implicit solvation model, which will be discussed in more detail in a future publication. Note that the ligand contains both nitrogen (N) and sulfur (S) atoms. Interestingly, both show enhanced interactions with specific silver (Ag) atoms on the $[Ag_{29}]^{3-}$ NC when **L′** is positioned to allow this (see Figure S8). The strongest interaction found (ca. 0.75 eV overall binding energy, see Figure 5) occurs when the secondary ligand is oriented *tangentially* to the ligand shell of $[Ag_{29}]^{3-}$ NC such that an S atom in the terminal SH group of the **L′** ligand can optimally interact with a tetrahedral Ag site on the NC (by contrast, radial attachment or partial radial insertion into the preexisting L ligand shell is found to be highly unfavorable; see Figure S8). This configuration is schematically shown in Figure 5A(ii) and depicted in more detail in Figures S7 and S8. Note that tangential binding of **L′** to undercoordinated Ag atoms at crown sites was found to be less favorable than to tetrahedral sites. Binding of **L′** to tetrahedral Ag sites allows the additional $\pi\cdots\pi$ stacking interaction between **L′** and L ligands (see Figure 6). A related noncovalent interaction between a fullerene secondary ligand and $[Ag_{29}]^{3-}$ was observed in a previous report.[32] Based on the optimal **L′** bonding orientation found for $[Ag_{29}]L'^{3-}$, we also constructed structural models for $[Ag_{29}]L'_{2-4}{}^{3-}$ (addition of further **L′** ligands tangentially and keeping them as far apart as possible). CCS_{N2} values simulated on the basis of these models (using DFT + TM; Figure 5A(ii−v),5B) show a linear increase with the number of **L′** added as plotted in Figure 4B—in good qualitative agreement with the experiment. Predicted $^{Cal}CCS_{N2}$ values were however found to depend quite sensitively on the (relative) orientations of **L′**. Furthergoing studies (also including systematic docking simulations of higher numbers of secondary ligands onto $[Ag_{29}]^{3-}$ NC) will be reported elsewhere.

Beyond the predicted linear increase in $^{Cal}CCS_{N2}$ with the number of secondary ligands added, it is also instructive to examine the changes to the precursor $[Ag_{29}]^{3-}$ NC structure upon **L′** attachment. Figures 6, S9, and S10 provide the corresponding details of the DFT-optimized structures (including calculated root-mean-square displacement (RMSD) values). The $Ag_{core} - Ag_{ico}$ bond length of ∼2.83 Å in the $[Ag_{29}]^{3-}$ NC remains essentially the same at ∼2.81 Å in $[Ag_{29}]L'_4{}^{3-}$. By contrast, the average $Ag_{core} - Ag_{crown}$ bond length in $[Ag_{29}]^{3-}$ NC is significantly increased during **L′**-attachments (∼4.64 Å), compared to the $[Ag_{29}]^{3-}$ (∼4.52 Å). Changes in Ag−Ag atomic distances (Å) in $[Ag_{29}]L'_4{}^{3-}$ as a function of bond index (i.e., variation of individual $Ag_{ico/crown} - Ag_{core}$ bond lengths of the NC before and after the **L′** incorporation) and the distances between L ligands are shown in Figure S10 and Figure 7, respectively.

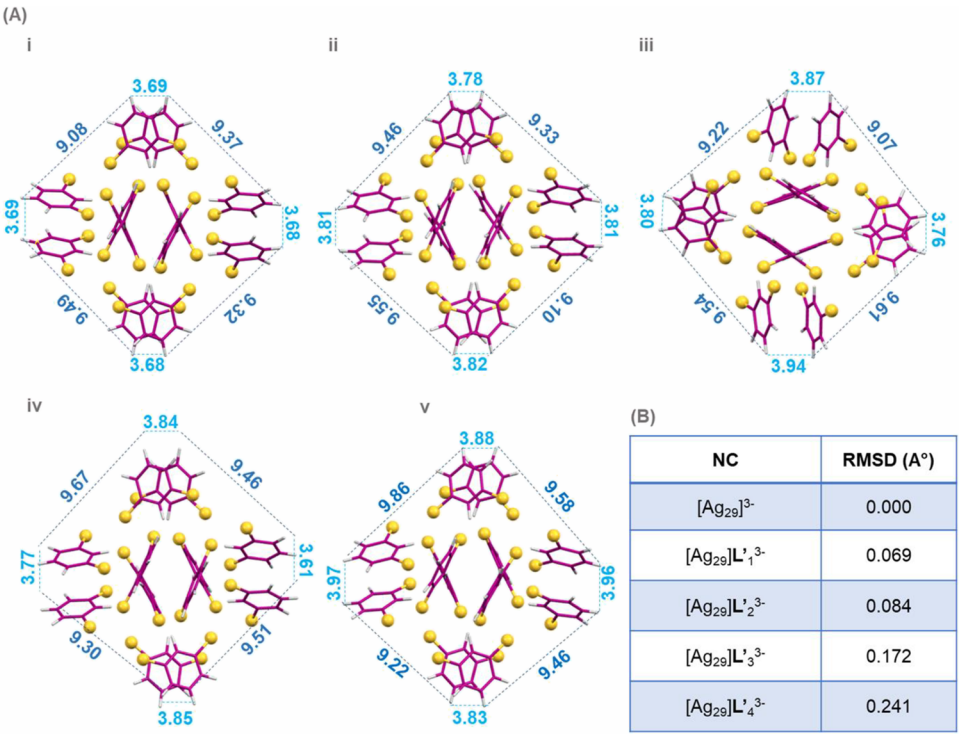

(B)

NC	RMSD (A°)
$[Ag_{29}]^{3-}$	0.000
$[Ag_{29}]L'_1{}^{3-}$	0.069
$[Ag_{29}]L'_2{}^{3-}$	0.084
$[Ag_{29}]L'_3{}^{3-}$	0.172
$[Ag_{29}]L'_4{}^{3-}$	0.241

Figure 7. Reduced representations of DFT-derived minimum energy structures for $[Ag_{29}]L'_n{}^{3-}$ NC, n = 0−4 (i−v) depicted in Figure 5 (here, the Ag_{29} core and the L′ ligands have been removed from the $[Ag_{29}]L'_n{}^{3-}$ structures for clarity). This representation highlights changes to the Ag−S staple and ligand L orientation upon incorporation of L′ into the parent $[Ag_{29}]^{3-}$. Shown are (A) distances between different L ligands attached to Ag−S staples in the DFT-optimized structure of $[Ag_{29}]L'_n{}^{3-}$ NC, n = 0−4 (i−v). Color codes: light blue denotes the distance measured between two pairs of parallel Ls; dark blue denotes the distance between terminal Hs of two parallel Ls. All distances are given in Å. (B) Root-mean-square displacement (RMSD) of silver atoms in L′-$[Ag_{29}]^{3-}$ adduct ions from the parent $[Ag_{29}]^{3-}$ ion calculated as indicated in the text. Color code: S, yellow; C, dark magenta; and H, light gray. Overall, L′ complexation leads to the expansion of Ag−S staples and to associated changes in positions/extensions of the 12 L ligands.

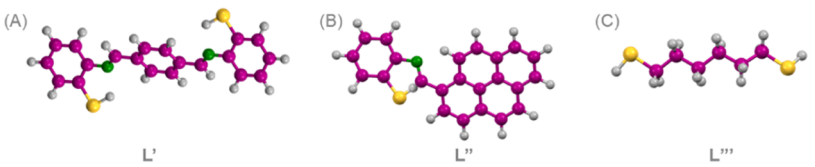

Figure 8. Schematic structures of (A) L′, (B) L″, and (C) L‴. Color code: S, yellow; C, dark magenta; and H, light gray.

We infer that upon attachment of **L′**, the proximal Ag−S staple framework of the NC precursor expands, and correspondingly, the distance between adjacent L-pairs increases (see Figure 6 for further details). Compared to the parent $[Ag_{29}]^{3-}$ NC, $[Ag_{29}]L'_n{}^{3-}$ ions not only have larger ${}^{Cal}CCS_{N2}$ because of the added secondary ligands, they are also larger because **L′** complexation causes the $[Ag_{29}]^{3-}$ NC precursor to noticeably expand. This ultimately reflects an enhanced $\pi\cdots\pi$ stacking[77] interaction between **L′** and L ligands as well an ionic contribution resulting from charge transfer between terminal SH and axial Ag atoms on the NC as the detail in Figure 6 shows.

In analogous calculations of adducts of the $[Ag_{29}]^{3-}$ NC with the other two structurally similar secondary ligands screened in this study (**L″** and **L‴**, see Figure 8), we found no significant structural changes of the central $[Ag_{29}]^{3-}$ NC consistent with no detectable adduct formation in the experiment (see Figure S11). The calculated binding energies of **L″** and **L‴** ligands on $[Ag_{29}]^{3-}$ NC were −0.58 and −0.71 eV, respectively. This observation highlights the highly specific interaction of **L′** with the $[Ag_{29}]^{3-}$ NC, which leads to a significant restructuring of its surface.

CONCLUSIONS

We have studied the interaction between the secondary dithiol ligand **L′** = 2,2′-[1,4-phenylenebis(methylidynenitrilo)] bis-[benzenethiol] and the atomically precise silver cluster $[Ag_{29}(L)_{12}]^{3-}$ (L = 1,3-benzene-dithiol). Our results imply a specific interaction between the secondary ligand and $[Ag_{29}]^{3-}$ NC, leading to facile formation of a series of noncovalently bound adducts $[Ag_{29}]L'_n{}^{3-}$. DFT calculations indicate that this is also associated with a progressive volume expansion of the $[Ag_{29}]^{3-}$ precursor as secondary ligands are added. Our ion mobility measurements (IMS MS and MS^2 IMS) provide further support for this interpretation. Upon electrospray ionization, $[Ag_{29}]L'_n{}^{3-}$, can be transferred intactly into the gas phase and subsequently collisionally dissociated. In the studies of adducts with n ≤ 4, we found loss of neutral **L′** to be the primary (and lowest energy) fragmentation channel, consistent with DFT-computed secondary ligand binding energies of < 1 eV (see Figure 7B). In all cases, $[Ag_{29}]L'_{n-m}{}^{3-}$ fragments

(thermalized to room temperature after having lost many $\mathbf{L}'$ secondary ligands) were found to have *larger* ^{TW}CCS than equi-mass ions, which had not undergone fragmentation. Apparently, these "footprints" of previously bound $\mathbf{L}'$ can survive in the gas phase on the time scale of the ion mobility measurement (ca. 1 ms). Perhaps, this time is too short to allow these isomers to return to their parent structure.

Although our study was centered around secondary ligand-induced structural distortion of $[Ag_{29}]^{3-}$ NCs, our methods and results are applicable to extremely fast ligand interactions of metal NCs in general. In this system, we have recently looked at higher $\mathbf{L}'$ coverages and interlinked dimers and will report the results in a separate contribution.

EXPERIMENTAL SECTION

ESI MS and IM MS Measurements. High-resolution ESI MS, IMS MS, and MS^2 IMS measurements were performed using two different ion mobility mass spectrometers, namely, a Synapt G2-Si HDMS (Waters, Manchester, U.K.) at IIT Madras and a timsTOF (Bruker Daltonics, Bremen, Germany) at KIT. The timsTOF was used to obtain high-resolution mobility data for the parent ions directly sprayed from solution (IMS MS), whereas the Synapt allowed us to also study charged fragments but at somewhat reduced mobility resolution (MS^2 IMS). The Synapt instrumental platform comprises a combination of quadrupole mass filter, TWIMS, and time-of-flight mass spectrometer, which allow separation of ions according to their CCS ($^{TW}CCS_{N2}$; with a resolution of ~40 ($^{TW}CCS_{N2}/\Delta\,^{TW}CCS_{N2}$) in terms of full width at half maximum, FWHM) and mass-to-charge ratio, m/z. The trap and transfer were filled with argon (Ar) with a flow rate of 3 mL/min (p = ~0.006 mbar),[78] whereas the TWIMS cell was filled with N_2 (40 mL/min).[79] All samples were measured in negative electrospray ionization mode. The mass scale of the instrument was calibrated by using NaI cluster ions. Typical experimental parameters were as follows: desolvation gas temperature: 150 °C, source temperature: 100 °C, desolvation gas flow: 400 L/h, capillary voltage: 3 kV, sample cone: 10−20 V, source offset: 0−20 V, trap collision energy: 2−30 V, trap gas flow: 2 mL/min, helium cell gas flow: 90−150 mL/min, IMS gas flow: 60−80 mL/min, trap DC bias: 28−45 V; IMS wave height: 38 V, and IMS wave velocity: 550 m/s. The collision voltage in the trap cell was raised until fragmentation of the selected ion was initiated (typically CE = 2−30 V). The sample concentration was 1 μg/mL (in DMF−methanol solvent mixture) and infused at a flow rate of 20 μL/min. Polyalanine ions were used for calibrating the $^{TW}CCS_{N_2}$ values (correcting for charge state) and were measured under the same experimental conditions as $[Ag_{29}]^{3-}$ ions. The $^{TW}CCS_{N_2}$ value of the $[Ag_{29}]^{3-}$ NC was consistent with the previous literature determination (see also below).[39] Data processing was conducted by using Waters Masslynx 4.1 and DriftScope 2.1.

The timsTOF platform was used to determine ion mobilities with a particularly high accuracy and resolution. In timsTOF, electrosprayed ions are separated according to their $^{TIMS}CCS_{N2}$ in a trapped ion mobility cell (typical resolution: ~200 ($^{TIMS}CCS_{N2}/\Delta^{TIMS}CCS_{N2}$)) followed by mass separation in a time-of-flight mass spectrometer (i.e., no mass selection prior to the IMS separation). ESI MS and IMS MS measurements in timsTOF were recorded in negative ion mode under the following experimental conditions. ESI flow rate: 100 μL/h, capillary voltage: 5 kV, end plate offset: 2200 V, nebulizer gas flow: 0.3 bar, dry gas: 3 L/min, dry temperature: 200 °C, and TIMS delta values ($\Delta1$ − $\Delta6$): 100, 100, −80, −50, 5, and −100 V. Other parameters and CCS_{N2} calibration procedures were as described previously.[80]

Despite the different ESI sources and spray conditions used, mass spectra were in qualitative agreement across the two different instrumental platforms.

Computational Details. All DFT-based calculations were carried out using the projector augmented wave (PAW) method as implemented in the Vienna *Ab initio* Simulation Package (VASP).[81] The electronic exchange and correlation interactions have been integrated utilizing the generalized gradient approximation of Perdew−Burke−Ernzerhof (GGA-PBE) functional.[82] The conjugate gradient algorithm has been considered for ionic relaxation with electronic energy and force criteria set to 10^{-4} eV and 0.05 eV/Å (Hellmann−Feynman forces on atoms), respectively. The plane wave cutoff energy has been set to 470 eV to enlarge the electronic wave function. $A \sim 8$ Å vacuum was set along all directions to avoid possible interactions between periodic images. As the unit cells of the compounds were rather large, we sampled the Brillouin zone at the 1 × 1 × 1 Γ k-point mesh.

CCS Calculations. The CCS was calculated for DFT-derived structural models using the trajectory method (TM) as implemented in IMoS 1.10.[32,83] For each structure considered, we typically ran 4,500,000 trajectories.[39] In order to investigate changes in Ag−Ag bond distances as a result of $\mathbf{L}'$ addition to $[Ag_{29}]^{3-}$ NC, the resulting RMSD of the 16 staple Ag atoms from the central Ag atom of NC ions was calculated following the equation[84]

$$\mathrm{RMSD} = \sqrt{\frac{1}{N}\sum_{j=1,m}(da_j - db_j)^2}$$

where da_j and db_j are the distances between the staple Ag atom (j = m) and central Ag atom (j = 1) in $[Ag_{29}]^{3-}$ and $[Ag_{29}]\mathbf{L}'_n{}^{3-}$ NC ions, respectively.

AUTHOR INFORMATION

Corresponding Authors

Biswarup Pathak − *Department of Chemistry, Indian Institute of Technology Indore, Indore 453552, India;* orcid.org/0000-0002-9972-9947; Email: biswarup@iiti.ac.in

Manfred M. Kappes − *Institute of Nanotechnology, Karlsruhe Institute of Technology (KIT), 76131 Karlsruhe, Germany; Institute of Physical Chemistry, Karlsruhe Institute of Technology (KIT), 76131 Karlsruhe, Germany;* orcid.org/0000-0002-1199-1730; Email: manfred.kappes@kit.edu

Thalappil Pradeep − *DST Unit of Nanoscience (DST UNS) & Thematic Unit of Excellence (TUE), Department of Chemistry, Indian Institute of Technology Madras, Chennai 600036, India; International Centre for Clean Water, Chennai 600113, India;* orcid.org/0000-0003-3174-534X; Email: pradeep@iitm.ac.in; Fax: 91-44-2257-0545/0509

Authors

Jayoti Roy − *DST Unit of Nanoscience (DST UNS) & Thematic Unit of Excellence (TUE), Department of Chemistry, Indian Institute of Technology Madras, Chennai 600036, India*

Amitabha Das − *Department of Chemistry, Indian Institute of Technology Indore, Indore 453552, India;* orcid.org/0000-0002-5000-4451

Arijit Jana − *DST Unit of Nanoscience (DST UNS) & Thematic Unit of Excellence (TUE), Department of*

Chemistry, Indian Institute of Technology Madras, Chennai 600036, India

Papri Chakraborty − *Institute of Nanotechnology, Karlsruhe Institute of Technology (KIT), 76131 Karlsruhe, Germany; Institute of Physical Chemistry, Karlsruhe Institute of Technology (KIT), 76131 Karlsruhe, Germany;* orcid.org/0000-0002-1353-7734

Marco Neumaier − *Institute of Nanotechnology, Karlsruhe Institute of Technology (KIT), 76131 Karlsruhe, Germany; Institute of Physical Chemistry, Karlsruhe Institute of Technology (KIT), 76131 Karlsruhe, Germany;* orcid.org/0000-0002-3810-3377

Horst Hahn − *Institute of Nanotechnology, Karlsruhe Institute of Technology (KIT), 76131 Karlsruhe, Germany; School of Sustainable Chemical, Biological and Materials Engineering, The University of Oklahoma, Norman 73019-1004 Oklahoma, United States*

Notes

The authors declare no competing financial interest.

ACKNOWLEDGMENTS

The authors thank the Department of Science and Technology (DST), Gov ernment of India, for constantly supporting our research program. J.R. and A.J. thank IIT Madras for an institute doctoral fellowship. J.R. also acknowledges partial support by the Gunther-Schroff Foundation. T.P. acknowledges funding from the Centre of Excellence on Molecular Materials and Functions under the Institution of Eminence scheme of IIT Madras. T.P. also acknowledges the Science and Engineering Research Board (SERB) for a J.C. Bose Fellowship (CHY1516331DSTXTPRA) and a Scientific and Useful Profound Research Advancement research grant (SP22230413CYSERB002505). He also thanks the DST for a research grant from the Indo-German Collaborative Activities in Chemistry and Physics scheme (SP20210994CYDSTX002505). M.K. and H.H. thank the German Science Foundation (DFG) for support of a DFG-DST collaborative project under KA 972/11-1 and HA 1344/ 47-1.

REFERENCES

(1) Pradeep, T. *Atomically Precise Metal Nanoclusters*, 1st ed.; Elsevier, 2023.

(2) Kang, X.; Chong, H.; Zhu, M. $Au_{25}(SR)_{18}$: The Captain of the Great Nanocluster Ship. *Nanoscale* **2018**, *10*, 10758−10834.

(3) Kang, X.; Zhu, M. Transformation of Atomically Precise Nanoclusters by Ligand-Exchange. *Chem. Mater.* **2019**, *31* (24), 9939−9969.

(4) Du, Y.; Sheng, H.; Astruc, D.; Zhu, M. Atomically Precise Noble Metal Nanoclusters as Efficient Catalysts: A Bridge between Structure and Properties. *Chem. Commun.* **2020**, *120* (2), 526−622.

(5) Cai, J.; Javed, R.; Ye, D.; Zhao, H.; Zhang, J. Recent Progress in Noble Metal Nanocluster and Single Atom Electrocatalysts for the Hydrogen Evolution Reaction. *J. Mater. Chem. A* **2020**, *8* (43), 22467−22487.

(6) Zhang, L.; Wang, E.; Wang, E. ScienceDirect Metal Nanoclusters: New Fluorescent Probes for Sensors and Bioimaging. *Nano Today* **2014**, *9*, 132−157.

(7) Bergamaschi, G.; Metrangolo, P.; Dichiarante, V. Photoluminescent Nanocluster-Based Probes for Bioimaging Applications. *Photochem. Photobiol. Sci.* **2022**, *21* (5), 787−801.

(8) Yang, G.; Wang, Z.; Du, F.; Jiang, F.; Yuan, X.; Ying, J. Y. Ultrasmall Coinage Metal Nanoclusters as Promising Theranostic Probes for Biomedical Applications. *J. Am. Chem. Soc.* **2023**, *145*, 11879−11898.

(9) Negishi, Y.; Takasugi, Y.; Sato, S.; Yao, H.; Kimura, K.; Tsukuda, T. Magic-Numbered Au_n Clusters Protected by Glutathione Monolayers (n = 18, 21, 25, 28, 32, 39): Isolation and Spectroscopic Characterization. *J. Am. Chem. Soc.* **2004**, *126* (21), 6518−6519.

(10) Qian, J.; Yang, Z.; Lyu, J.; Yao, Q.; Xie, J. Molecular Interactions in Atomically Precise Metal Nanoclusters. *Precis. Chem.* **2024**, *2* (10), 495−517.

(11) Gholipour-Ranjbar, H.; Sertse, L.; Forbes, D.; Laskin, J. Effect of Ligands on the Reactivity of the Undercoordinated Fragment Ions of $Co_6S_8(PEt_{3-X}Ph_x)_6^+$ (x = 0−3) Clusters on Surfaces. *J. Phys. Chem. C* **2024**, *128* (20), 8232−8238.

(12) Fei, W.; Antonello, S.; Dainese, T.; Dolmella, A.; Lahtinen, M.; Rissanen, K.; Venzo, A.; Maran, F. Metal Doping of $Au_{25}(SR)_{18}^-$ Clusters: Insights and Hindsights. *J. Am. Chem. Soc.* **2019**, *141* (40), 16033−16045.

(13) Kang, X.; Wei, X.; Jin, S.; Yuan, Q.; Luan, X.; Pei, Y.; Wang, S.; Zhu, M.; Jin, R. Rational Construction of a Library of M_{29} Nanoclusters from Monometallic to Tetrametallic. *Proc. Natl. Acad. Sci. U.S.A.* **2019**, *116* (38), 18834−18840.

(14) Jadzinsky, P. D.; Calero, G.; Ackerson, C. J.; Bushnell, D. A.; Kornberg, R. D. Structure of a Thiol Monolayer-Protected Gold Nanoparticle at 1.1 Å Resolution. *Science* **2007**, *318* (5849), 430−433.

(15) Yang, H.; Wang, Y.; Chen, X.; Zhao, X.; Gu, L.; Huang, H.; Yan, J.; Xu, C.; Li, G.; Wu, J.; Edwards, A. J.; Dittrich, B.; Tang, Z.; Wang, D.; Lehtovaara, L.; Häkkinen, H.; Zheng, N. Plasmonic Twinned Silver Nanoparticles with Molecular Precision. *Nat. Commun.* **2016**, *7*, No. 12809.

(16) Mondal, B.; Jana, A.; Roy, J.; Mata, A. C.; Nair, A. S.; Mahendranath, A.; Roy, S.; Pathak, B.; Ajayan, P. M.; Pradeep, T. Structure and Electrocatalytic Performance of Cocrystallized Ternary Molybdenum Oxosulfide Clusters for Efficient Water Splitting. *ACS Mater. Lett.* **2023**, *5* (12), 3306−3315.

(17) Wei, X.; Chu, K.; Adsetts, J. R.; Li, H.; Kang, X.; Ding, Z.; Zhu, M. Nanocluster Transformation Induced by SbF6-Anions toward Boosting Photochemical Activities. *J. Am. Chem. Soc.* **2022**, *144* (44), 20421−20433.

(18) Song, Y.; Lambright, K.; Zhou, M.; Kirschbaum, K.; Xiang, J.; Xia, A.; Zhu, M.; Jin, R. Large-Scale Synthesis, Crystal Structure, and Optical Properties of the $Ag_{146}Br_2(SR)_{80}$ Nanocluster. *ACS Nano* **2018**, *12* (9), 9318−9325.

(19) Roy, J.; Mondal, B.; Vishwakarma, G.; Nonappa; Sridharan, N. V.; Krishnamurthi, P.; Pradeep, T. Dissociative Reactions of $[Au_{25}(SR)_{18}]^-$ at Copper Oxide Nanoparticles and Formation of Aggregated Nanostructures. *Nanoscale* **2023**, *15* (18), 8225−8234.

(20) Wei, X.; Kang, X.; Jin, S.; Wang, S.; Zhu, M. Aggregation of Surface Structure Induced Photoluminescence Enhancement in Atomically Precise Nanoclusters. *CCS Chem.* **2021**, *3* (7), 1929−1939.

(21) Jana, A.; Jash, M.; Dar, W. A.; Roy, J.; Chakraborty, P.; Paramasivam, G.; Lebedkin, S.; Kirakci, K.; Manna, S.; Antharjanam, S.; Machacek, J.; Kucerakova, M.; Ghosh, S.; Lang, K.; Kappes, M. M.; Base, T.; Pradeep, T. Carborane-Thiol Protected Copper Nanoclusters: Stimuli-Responsive Materials with Tunable Phosphorescence. *Chem. Sci.* **2023**, *14* (6), 1613−1626.

(22) Jadzinsky, P. D.; Calero, G.; Ackerson, C. J.; Bushnell, D. A.; Kornberg, R. D. Structure of a Thiol Monolayer-Protected Gold Nanoparticle at 1.1 Å Resolution. *Science* **2007**, *318* (5849), 430−433.

(23) Guo, J.; Kumar, S.; Bolan, M.; Desireddy, A.; Bigioni, T. P.; Griffith, W. P. Mass Spectrometric Identification of Silver Nanoparticles: The Case of $Ag_{32}(SG)_{19}$. *Anal. Chem.* **2012**, *84* (12), 5304−5308.

(24) Hirata, K.; Chakraborty, P.; Nag, A.; Takano, S.; Koyasu, K.; Pradeep, T.; Tsukuda, T. Interconversions of Structural Isomers of $[PdAu_8(PPh_3)_8]^{2+}$ and $[Au_9(PPh_3)_8]^{3+}$ Revealed by Ion Mobility Mass Spectrometry. *J. Phys. Chem. C* **2018**, *122* (40), 23123−23128.

(25) Baksi, A.; Chakraborty, P.; Bhat, S.; Natarajan, G.; Pradeep, T. [Au25(SR)18]22−: A Noble Metal Cluster Dimer in the Gas Phase. *Chem. Commun.* **2016**, *52*, 8397−8400.
(26) Wang, Y.; Nieto-Ortega, B.; Bürgi, T. Amplification of Enantiomeric Excess by Dynamic Inversion of Enantiomers in Deracemization of Au_{38} Clusters. *Nat. Commun.* **2020**, *11*, No. 4562.
(27) Ligare, M. R.; Reveles, J. U.; Govind, N.; Johnson, G. E.; Laskin, J. Influence of Interligand Interactions and Core-Charge Distribution on Gold Cluster Stability: Enthalpy Versus Entropy. *J. Phys. Chem. C* **2019**, *123* (40), 24899−24911.
(28) Krishnadas, K. R.; Baksi, A.; Ghosh, A.; Natarajan, G.; Pradeep, T. Manifestation of Geometric and Electronic Shell Structures of Metal Clusters in Intercluster Reactions. *ACS Nano* **2017**, *11*, 6015−6023.
(29) Salassa, G.; Krishnadas, K. R.; Pupier, M.; Viger-Gravel, J.; Bürgi, T. Role of Intercluster and Interligand Dynamics of $[Ag_{25}(DMBT)_{18}]^-$ Nanoclusters by Multinuclear Magnetic Resonance Spectroscopy. *J. Phys. Chem. C* **2021**, *125* (4), 2524−2530.
(30) Ligare, M. R.; Baker, E. S.; Laskin, J.; Johnson, G. E. Ligand Induced Structural Isomerism in Phosphine Coordinated Gold Clusters Revealed by Ion Mobility Mass Spectrometry. *Chem. Commun.* **2017**, *53*, 7389−7392.
(31) Nag, A.; Pradeep, T. Assembling Atomically Precise Noble Metal Nanoclusters Using Supramolecular Interactions. *ACS Nanosci. Au* **2022**, *2* (3), 160−178.
(32) Chakraborty, P.; Nag, A.; Paramasivam, G.; Natarajan, G.; Pradeep, T. Fullerene-Functionalized Monolayer-Protected Silver Clusters: $[Ag_{29}(BDT)_{12}(C_{60})_n]^{3-}$ (n = 1−9). *ACS Nano* **2018**, *12* (3), 2415−2425.
(33) Knoppe, S.; Bürgi, T. The Fate of Au25(SR)18 Clusters upon Ligand Exchange with Binaphthyl-Dithiol: Interstaple Binding vs. Decomposition. *Phys. Chem. Chem. Phys.* **2013**, *15* (38), 15816−15820.
(34) Malola, S.; Häkkinen, H. Chiral Inversion of Thiolate-Protected Gold Nanoclusters via Core Reconstruction without Breaking a Au−S Bond. *J. Am. Chem. Soc.* **2019**, *141* (14), 6006−6012.
(35) Wang, Y.; Bürgi, T. Ligand Exchange Reactions on Thiolate-Protected Gold Nanoclusters. *Nanoscale Adv.* **2021**, *3* (10), 2710−2727.
(36) Ghosh, A.; Ghosh, D.; Khatun, E.; Chakraborty, P.; Pradeep, T. Unusual Reactivity of Dithiol Protected Clusters in Comparison to Monothiol Protected Clusters: Studies Using $Ag_{51}(BDT)_{19}(TPP)_3$ and $Ag_{29}(BDT)_{12}(TPP)_4$. *Nanoscale* **2017**, *9* (3), 1068−1077.
(37) Tang, L.; Kang, X.; Wang, X.; Zhang, X.; Yuan, X.; Wang, S. Dynamic Metal Exchange between a Metalloid Silver Cluster and Silver(I) Thiolate. *Inorg. Chem.* **2021**, *60*, 3037−3045.
(38) Bootharaju, M. S.; Kozlov, S. M.; Cao, Z.; Harb, M.; Parida, M. R.; Hedhili, M. N.; Mohammed, O. F.; Bakr, O. M.; Cavallo, L.; Basset, J.-M. Direct versus Ligand-Exchange Synthesis of $[PtAg_{28}(BDT)_{12}(TPP)_4]^{4-}$ Nanoclusters: Effect of a Single-Atom Dopant on the Optoelectronic and Chemical Properties †. *Nanoscale* **2017**, *9*, 9529−9536, DOI: 10.1039/c7nr02844j.
(39) Zeng, Y.; Havenridge, S.; Gharib, M.; Baksi, A.; Weerawardene, K. L. D. M.; Ziefuß, A. R.; Strelow, C.; Rehbock, C.; Mews, A.; Barcikowski, S.; Kappes, M. M.; Parak, W. J.; Aikens, C. M.; Chakraborty, I. Impact of Ligands on Structural and Optical Properties of Ag_{29} Nanoclusters. *J. Am. Chem. Soc.* **2021**, *143* (25), 9405−9414.
(40) Matus, M. F.; Häkkinen, H. Understanding Ligand-Protected Noble Metal Nanoclusters at Work. *Nat. Rev. Mater.* **2023**, *8* (6), 372−389.
(41) Hazer, M. S. A.; Malola, S.; Häkkinen, H. Isomer Dynamics of the $[Au_6(NHC\text{-}S)_4]^{2+}$ Nanocluster. *Chem. Commun.* **2022**, *58* (19), 3218−3221.
(42) Matus, M. F.; Malola, S.; Bonilla, E. K.; Barngrover, B. M.; Aikens, C. M.; Häkkinen, H. A Topological Isomer of the $Au_{25}(SR)_{18}^-$ Nanocluster. *Chem. Commun.* **2020**, *56* (58), 8087−8090.
(43) Christofi, E.; Barran, P. Ion Mobility Mass Spectrometry (IM-MS) for Structural Biology: Insights Gained by Measuring Mass, Charge, and Collision Cross Section. *Chem. Rev.* **2023**, *123*, 2902−2949.
(44) Zhong, Y.; Hyung, S.-J.; Ruotolo, B. T. Ion Mobility−Mass Spectrometry for Structural Proteomics. *Expert Rev. Proteomics* **2012**, *9* (1), 47−58.
(45) Donor, M. T.; Mroz, A. M.; Prell, J. S. Experimental and Theoretical Investigation of Overall Energy Deposition in Surface-Induced Unfolding of Protein Ions. *Chem. Sci.* **2019**, *10* (14), 4097−4106.
(46) Vicent, C.; Martinez-Agramunt, V.; Gandhi, V.; Larriba-Andaluz, C.; Gusev, D. G.; Peris, E. Ion Mobility Mass Spectrometry Uncovers Guest-Induced Distortions in a Supramolecular Organometallic Metallosquare. *Angew. Chem., Int. Ed.* **2021**, *60* (28), 15412−15417.
(47) Gholipour-Ranjbar, H.; Deepika; Jena, P.; Laskin, J. Gas-Phase Fragmentation of Single Heteroatom-Incorporated Co5MS8(PEt3)6+ (M = Mn, Fe, Co, Ni) Nanoclusters. *Commun. Chem.* **2022**, *5* (1), No. 130.
(48) Baksi, A.; Schneider, E. K.; Weis, P.; Krishnadas, K. R.; Ghosh, D.; Hahn, H.; Pradeep, T.; Kappes, M. M. Nanogymnastics: Visualization of Intercluster Reactions by High-Resolution Trapped Ion Mobility Mass Spectrometry. *J. Phys. Chem. C* **2019**, *123* (46), 28477−28485.
(49) Wu, R.; Metternich, J. B.; Tiwari, P.; Benzenberg, L. R.; Harrison, J. A.; Liu, Q.; Zenobi, R. Structural Studies of a Stapled Peptide with Native Ion Mobility-Mass Spectrometry and Transition Metal Ion Förster Resonance Energy Transfer in the Gas Phase. *J. Am. Chem. Soc.* **2022**, *144* (32), 14441−14445.
(50) Zhou, M.; Huang, C.; Wysocki, V. H. Surface-Induced Dissociation of Ion Mobility-Separated Noncovalent Complexes in a Quadrupole/Time-of-Flight Mass Spectrometer. *Anal. Chem.* **2012**, *84* (14), 6016−6023.
(51) Masike, K.; Stander, M. A.; de Villiers, A. Recent Applications of Ion Mobility Spectrometry in Natural Product Research. *J. Pharm. Biomed. Anal.* **2021**, *195*, No. 113846.
(52) Mu, Y.; Schulz, B.; Ferro, V. Applications of Ion Mobility-Mass Spectrometry in Carbohydrate Chemistry and Glycobiology. *Molecules* **2018**, *23* (10), No. 2557.
(53) Kang, X.; Zhu, M. Structural Isomerism in Atomically Precise Nanoclusters. *Chem. Mater.* **2021**, *33* (1), 39−62.
(54) Chakraborty, P.; Baksi, A.; Mudedla, S. K.; Nag, A.; Paramasivam, G.; Subramanian, V.; Pradeep, T. Understanding Proton Capture and Cation-Induced Dimerization of $[Ag_{29}(BDT)_{12}]^{3-}$ Clusters by Ion Mobility Mass Spectrometry. *Phys. Chem. Chem. Phys.* **2018**, *20*, 7593−7603.
(55) Baksi, A.; Ghosh, A.; Mudedla, S. K.; Chakraborty, P.; Bhat, S.; Mondal, B.; Krishnadas, K. R.; Subramanian, V.; Pradeep, T. Isomerism in Monolayer Protected Silver Cluster Ions: An Ion Mobility-Mass Spectrometry Approach. *J. Phys. Chem. C* **2017**, *121* (24), 13421−13427.
(56) Baksi, A.; Schneider, E. K.; Weis, P.; Chakraborty, I.; Fuhr, O.; Lebedkin, S.; Parak, W. J.; Kappes, M. M. Linear Size Contraction of Ligand Protected Ag_{29} Clusters by Substituting Ag with Cu. *ACS Nano* **2020**, *14* (11), 15064−15070.
(57) Ligare, M. R.; Morrison, K. A.; Hewitt, M. A.; Reveles, J. U.; Govind, N.; Hernandez, H.; Baker, E. S.; Clowers, B. H.; Laskin, J.; Johnson, G. E. Ion Mobility Spectrometry Characterization of the Intermediate Hydrogen-Containing Gold Cluster $Au_7(PPh_3)_7H_5^{2+}$. *J. Phys. Chem. Lett.* **2021**, *12* (10), 2502−2508.
(58) Hossain, S.; Imai, Y.; Suzuki, D.; Choi, W.; Chen, Z.; Suzuki, T.; Yoshioka, M.; Kawawaki, T.; Lee, D.; Negishi, Y. Elucidating Ligand Effects in Thiolate-Protected Metal Clusters Using $Au_{24}Pt(TBBT)_{18}$ as a Model Cluster. *Nanoscale* **2019**, *11* (45), 22089−22098.
(59) Gabelica, V.; Marklund, E. Fundamentals of Ion Mobility Spectrometry. *Curr. Opin. Chem. Biol.* **2018**, *42*, 51−59.

(60) AbdulHalim, L. G.; Bootharaju, M. S.; Tang, Q.; Del Gobbo, S.; AbdulHalim, R. G.; Eddaoudi, M.; Jiang, D.; Bakr, O. M. $Ag_{29}(BDT)_{12}(TPP)_4$: A Tetravalent Nanocluster. *J. Am. Chem. Soc.* **2015**, *137* (37), 11970−11975.
(61) Hennrich, F.; Ito, S.; Weis, P.; Neumaier, M.; Takano, S.; Tsukuda, T.; Kappes, M. M. Cyclic Ion Mobility of Doped $[MAu_{24}L_{18}]^{2-}$ Superatoms and Their Fragments (M = Ni, Pd and Pt; L = Alkynyl). *Phys. Chem. Chem. Phys.* **2024**, *26* (10), 8408−8418.
(62) Chakraborty, P.; Malola, S.; Weis, P.; Neumaier, M.; Schneider, E. K.; Häkkinen, H.; Kappes, M. M. Tailoring Vacancy Defects in Isolated Atomically Precise Silver Clusters through Mercury-Doped Intermediates. *J. Phys. Chem. Lett.* **2023**, *14* (51), 11659−11664.
(63) Baksi, A.; Schneider, E. K.; Weis, P.; Chakraborty, I.; Fuhr, O.; Lebedkin, S.; Parak, W. J.; Kappes, M. M. Linear Size Contraction of Ligand Protected Ag_{29} Clusters by Substituting AG with Cu. *ACS Nano* **2020**, *14* (11), 15064−15070.
(64) Sarbu, M.; Clemmer, D. E.; Zamfir, A. D. Ion Mobility Mass Spectrometry of Human Melanoma Gangliosides. *Biochimie* **2020**, *177* (8), 226−237.
(65) Baksi, A.; Chakraborty, P.; Bhat, S.; Natarajan, G.; Pradeep, T. $[Au_{25}(SR)_{18}]_2^{2-}$: A Noble Metal Cluster Dimer in the Gas Phase. *Chem. Commun.* **2016**, *52* (54), 8397−8400.
(66) Chakraborty, P.; Malola, S.; Neumaier, M.; Weis, P.; Häkkinen, H.; Kappes, M. M. Elucidating the Structures of Intermediate Fragments during Stepwise Dissociation of Monolayer-Protected Silver Clusters. *Angew. Chem., Int. Ed.* **2023**, *62*, No. e202305836, DOI: 10.1002/anie.202305836.
(67) Zeng, Y.; Havenridge, S.; Gharib, M.; Baksi, A.; Weerawardene, K. L. D. M.; Ziefuß, A. R.; Strelow, C.; Rehbock, C.; Mews, A.; Barcikowski, S.; Kappes, M. M.; Parak, W. J.; Aikens, C. M.; Chakraborty, I. Impact of Ligands on Structural and Optical Properties of Ag29 Nanoclusters. *J. Am. Chem. Soc.* **2021**, *143* (25), 9405−9414.
(68) Ahlrichs, R.; Bär, M.; Häser, M.; Horn, H.; Kölmel, C. Electronic Structure Calculations on Workstation Computers: The Program System Turbomole. *Chem. Phys. Lett.* **1989**, *162* (3), 165−169.
(69) Vosko, S. H.; Wilk, L.; Nusair, M. Accurate Spin-Dependent Electron Liquid Correlation Energies for Local Spin Density Calculations: A Critical Analysis. *Can. J. Phys.* **1980**, *58* (8), 1200−1211.
(70) Lecklider, T. Maintainng a Heathy Rhythm. *Endeavor Bus. Media LLC* **2011**, *50* (1), 36−39.
(71) Becke, A. D. Density-Functional Thermochemistry. III. The Role of Exact Exchange. *J. Chem. Phys.* **1993**, *98* (7), 5648−5652.
(72) Dirac, P. A. M. Quantum Mechanics of Many-Electron Systems. *Proc. R. Soc. London, Ser. A* **1929**, *123* (792), 714−733.
(73) Slater, J. C. A Simplification of the Hartree-Fock Method. *Phys. Rev.* **1951**, *81* (3), No. 385.
(74) Weigend, F.; Ahlrichs, R. Balanced Basis Sets of Split Valence, Triple Zeta Valence and Quadruple Zeta Valence Quality for H to Rn: Design and Assessment of Accuracy. *Phys. Chem. Chem. Phys.* **2005**, *7* (18), 3297−3305.
(75) Grimme, S.; Ehrlich, S.; Goerigk, L. Effect of the Damping Function in Dispersion Corrected Density Functional Theory. *J. Comput. Chem.* **2011**, *32* (7), 1456−1465.
(76) Grimme, S.; Antony, J.; Ehrlich, S.; Krieg, H. A Consistent and Accurate Ab Initio Parametrization of Density Functional Dispersion Correction (DFT-D) for the 94 Elements H-Pu. *J. Chem. Phys.* **2010**, *132* (15), No. 154104.
(77) Shen, H.; Xu, J.; Fu, Z.; Wei, X.; Kang, X.; Shi, W.; Zhu, M. Photoluminescence Quenching of Hydrophobic Ag_{29} Nanoclusters Caused by Molecular Decoupling during Aqueous Phase Transfer and EmissionRecovery through Supramolecular Recoupling. *Angew. Chem., Int. Ed.* **2024**, *63* (12), No. e202317995, DOI: 10.1002/ANIE.202317995.
(78) Roy, J.; Chakraborty, P.; Paramasivam, G.; Natarajan, G.; Pradeep, T. Gas Phase Ion Chemistry of Titanium−Oxofullerene with Ligated Solvents. *Phys. Chem. Chem. Phys.* **2022**, *24* (4), 2332−2343.
(79) May, J. C.; McLean, J. A. Ion Mobility-Mass Spectrometry: Time-Dispersive Instrumentation. *Anal. Chem.* **2015**, *87* (3), 1422−1436.
(80) Chakraborty, P.; Malola, S.; Weis, P.; Neumaier, M.; Schneider, E. K.; Häkkinen, H.; Kappes, M. M. Tailoring Vacancy Defects in Isolated Atomically Precise Silver Clusters through Mercury-Doped Intermediates. *J. Phys. Chem. Lett.* **2023**, *14* (51), 11659−11664.
(81) Hafner, J. Ab-Initio Simulations of Materials Using VASP: Density-Functional Theory and Beyond. *J. Comput. Chem.* **2008**, *29* (13), 2044−2078.
(82) Perdew, J. P.; Burke, K.; Ernzerhof, M. Generalized Gradient Approximation Made Simple. *Phys. Rev. Lett.* **1996**, *77* (18), No. 3865.
(83) Nag, A.; Chakraborty, P.; Paramasivam, G.; Bodiuzzaman, M.; Natarajan, G.; Pradeep, T. Isomerism in Supramolecular Adducts of Atomically Precise Nanoparticles. *J. Am. Chem. Soc.* **2018**, *140* (42), 13590−13593.
(84) Fang, K. C.; Weng, C. I. An Investigation into the Melting of Silicon Nanoclusters Using Molecular Dynamics Simulations. *Nanotechnology* **2005**, *16* (2), 250−256.